Pt-Decorated PdFe Nanoparticles as Methanol-Tolerant Oxygen Reduction Electrocatalyst

Jinhua Yang,[†] Weijiang Zhou,[‡,†] Chin Hsien Cheng,[†] Jim Yang Lee,[*,†,§] and Zhaolin Liu[§]

Department of Chemical and Biomolecular Engineering, National University of Singapore, 10 Kent Ridge Crescent, Singapore 119260, and Institute of Materials Research and Engineering, 3 Research Link, Singapore 117602

ABSTRACT The activity and selectivity of carbon-supported Pt-decorated PdFe nanoparticles in the oxygen reduction reaction (ORR) were investigated in the presence and absence of methanol. The Pt-decorated PdFe nanoparticles, which consist of a PdPt surface and a PdFe interior, were prepared by the galvanic reaction between PdFe/C alloy nanoparticles and $PtCl_4^{2-}$ in aqueous solution. The presence of a Pt-enriched surface after the replacement reaction was independently confirmed by several microstructural characterization techniques and cyclic voltammetry. The catalyst with such heterogeneous architecture is catalytically more active than a bulk PdFePt alloy catalyst with the same overall composition. The observed enhancements in catalyst performance can be attributed to the lattice strain effect between the shell and core components. The Pt-decorated PdFe (PdFe@PdPt/C) catalyst also compares favorably with a commercial Pt/C catalyst with four times as much Pt in terms of ORR activity, cost, and methanol tolerance.

KEYWORDS: galvanic replacement reaction • oxygen reduction reaction • core shell nanoparticles • direct methanol fuel cells

INTRODUCTION

Modern surface science studies and density functional theory (DFT) calculations have demonstrated the importance of catalyst surface composition and near surface structure in catalysis (1−4). This has given rise to the interest in exploring a heterogeneous core shell construction for the catalyst design, which has many perceived advantages (5−7). First of all, a core shell construction can leverage on the use of a low-cost metal core and a noble metal overlayer to greatly reduce the cost of the catalyst. Second, the strain caused by the lattice mismatch between the surface and core components may be used to modify the electronic properties of the surface metal atoms, most notably their d band centers, which affect the rates of one or more elementary steps in the overall catalysis (8−11). For example, Kibler et al. (8) and Adzic et al. (9) have investigated the catalytic activities of Pt and Pd monolayers on different metal substrates and reported tunability of catalytic activities by the strain between the outermost layer and the underlying substrate. However, these studies using pure Pt and Pd on single-crystal metal substrates are basic research in catalysis, and the method of preparation is not amenable to volume production. Furthermore, the reactions in these studies have also been greatly simplified to eliminate the interference from competing reactions, which is hardly the case in industrial catalysis.

In direct methanol fuel cells (DMFCs), the electrocatalytic reduction of oxygen on the cathode has to compete with the electrocatalytic oxidation of methanol which diffuses from the anode to the cathode through the polymer electrolyte membrane (PEM) (12, 13). Although Pt is one of the best oxygen reduction catalysts, its activity is not selective to the oxygen reduction reaction (ORR) and hence the crossover fuel can cause significant reduction of the fuel cell performance. A much higher loading of Pt is therefore used at the DMFC cathode than at the cathode of a hydrogen PEM fuel cell. Besides methanol crossover, there are also conscious efforts to reduce the amount of Pt used in the cathode catalyst. This can in principle be done by limiting Pt to a thin layer deposited on a base metal surface by ultrahigh-vacuum technique (6) or by chemical reactions such as surface metal galvanic displacement (4) and surface metal depletion gliding (14). Non-noble metal catalysts such as nitrogen-containing complexes of cobalt and iron (15) have also been proposed as Pt substitutes but their chemical instability in acid solutions and low intrinsic ORR activities even without the crossover fuel are significant disadvantages. Hence one of the objectives in the ongoing work on DMFC cathode catalysts is to search for alternatives with ORR activities as high as that of Pt and yet demonstrating good methanol tolerance.

Recently, Pd and Pd alloy catalysts have been found to exhibit good activities and methanol tolerance in the ORR (16−18) even though the intrinsic ORR activity of Pd is lower than that of Pt (19, 20). Herein, we report our experimental discovery that a Pt-decorated PdFe catalyst (PdFe@PdPt)

* Corresponding author. Tel: 65 6516 2899. Fax: 65 6779 1936. E-mail: cheleejy@nus.edu.sg.

Received for review September 15, 2009 and accepted November 24, 2009

† National University of Singapore.

‡ Current address: Engineering School, Temasek Polytechnic, 21 Tampines Avenue 1, Singapore 529757.

§ Institute of Materials Research and Engineering.

DOI: 10.1021/am900623e

consisting of a PdPt surface and a PdFe core could perform very well in the ORR. (For convenience of reference, the nanoparticles are abbreviated as PdFe@PdPt because of their structural similarity to core−shell nanoparticles with a PdPt shell and a PdFe core; although in the current case, the Pd atoms in the "shell" are derived from the "core".) Aside from an overall reduction in the Pt usage, the catalyst also outperformed a Pt/C catalyst as well as a homogeneous PdPtFe/C alloy catalyst of the same overall composition in the presence of methanol, all at the same catalyst loading (on a total metal basis). The addition of Fe to the core increases the tunability of the lattice parameter of the core and hence the degree of lattice mismatch between the core and shell components causing the strain effect. It also contributes to a further reduction of the catalyst cost. The Pt-decorated PdFe (PdFe@PdPt) electrocatalyst can be easily prepared from the galvanic replacement reaction between PdFe/C alloy nanoparticles and $PtCl_4^{2-}$ in aqueous solution. Because no extraneous reducing agent is used, the deposition of Pt occurs exclusively on the PdFe surface and no monometallic Pt nanoparticles are formed as a byproduct.

EXPERIMENTAL SECTION

Potassium tetrachloroplatinate (K_2PtCl_4), ferric(III) chloride hexahydrate ($FeCl_3 \cdot 6H_20$), and 5 wt % Nafion in an ethanol−water mixture (containing 15−20% water) were purchased from Adrich-Sigma. 70−72% perchloric acid ($HClO_4$) and 99.8% methanol were supplied by Merck and Fisher Scientific respectively. Commercial carbon-supported platinum and palladium catalysts with 20 wt % metal were supplied by E-TEK. A JEOL JEM2010 field-emission transmission electron microscope was used for transmission electron microscopy (TEM) and high-resolution TEM (HRTEM) characterizations of the catalyst nanoparticles. The catalyst composition was determined in situ by an energy-dispersive X-ray spectroscopy (EDX) attachment to the microscope. Powder X-ray diffraction (XRD) patterns were recorded on a Rigaku D/Max-3B diffractometer, using Cu Kα radiation ($\lambda = 1.54056$ Å). X-ray photoelectron spectra (XPS) were obtained from an ESCALAB MKII spectrometer (VG Scientific) using Al Kα radiation (1486.71 eV).

Preparation of Electrocatalysts. Carbon-supported PdFe nanoparticles with a Pd:Fe mole ratio of 70:30 were prepared as follows: 40 mg of Pd/C and 3.21 mL of 10 mM $FeCl_3 \cdot 6H_2O$ were added to 50 mL of water and ultrasonically mixed for 30 min. The solution was then heated to 110 °C to evaporate away most of the water until a thick and smooth slurry was formed. The slurry, after being dried in a vacuum overnight, was placed in a glazed ceramic boat and heated in a tube furnace at 500 °C for 2 h in a flowing mixture of 5% hydrogen in argon (0.2 mL min^{-1}). The furnace was then cooled in flowing argon (0.1 mL min^{-1}) to room temperature Carbon-supported PdPtFe alloy nanoparticles with a Pt:Pd:Fe mole ratio of 12:70:18 were similarly prepared from a mixture of Pd/C, $FeCl_3 \cdot 6H_2O$, and K_2PtCl_4. On the other hand, PdFe@PdPt/C was prepared by the galvanic replacement reaction. In brief, the PdFe/C synthesized above was suspended in 50 mL of deionized water and refluxed at 100 °C under an argon blanket; 1.2 mL 10 mM K_2PtCl_4 diluted to 10 mL with deionized water was then added dropwise to the suspension and left to react for 2 h. The solid product that remained at the end of the reaction was recovered by centrifugation and dried in a vacuum overnight.

Electrochemical Measurement. Electrochemical measurements were carried out in a standard three-electrode cell. A Pt gauze and a Ag/AgCl (3 M KCl) electrode were used as the counter electrode and the reference electrode respectively. A thin layer of Nafion-impregnated catalyst cast on a vitreous carbon disk was used as the working electrode. A calculated volume of the catalyst ink (10 mg of ultrasonically dispersed catalyst in 10 mL o faqueous solution containing 4 mL of isopropanol and 0.1 mL of 5 wt % Nafion solution) was dispensed onto a 5 mm glassy carbon disk electrode to produce a nominal catalyst loading of 20.4 μg (Pt+Pd) per cm^2 of the electrode projection area. All potentials were converted to the reversible hydrogen electrode (RHE) scale and current densities were normalized by the projection area of the 5 mm diameter electrode. Pristine ORR activities were measured in 0.1 M $HClO_4$ electrolyte, whereas a solution of 0.1 M methanol in 0.1 M $HClO_4$ was used for the evaluation of methanol tolerance. Negative-going linear sweep voltammograms were recorded from 1.0 to 0.3 V at 20 mV s^{-1} at room temperature (22 ± 0.5 °C). Cyclic voltammograms were also recorded between 0 and 1.2 V at 20 mV s^{-1} at room temperature in 0.1 M $HClO_4$ for the measurement of electrochemically active surface areas.

RESULTS AND DISCUSSION

Electrocatalyst Characterizations. The deposition of Pt was spontaneous on PdFe surface because the equilibrium electrode potential of the $PtCl_4^{2-}$/Pt couple (1.249 V) is more positive than the equilibrium electrode potentials of Fe^{2+}/Fe (−0.669 V) and Pd^{2+}/Pd (0.729 V) couples (21). The greater potential difference between the $PtCl_4^{2-}$/Pt couple and the Fe^{2+}/Fe couple drove the preferential displacement of Fe (instead of Pd) by Pt, forming the heterogeneous structure of a PdPt surface on a PdFe core.

Figure 1 shows the TEM and HRTEM images of PdFe/C, PdPtFe/C and PdFe@PdPt/C catalysts. The PdFe@PdPt/C catalyst was selected from a series of previous measurements (see the Supporting Information) and the PdPtFe/C catalyst was designed to have the same overall metal distribution as PdFe@PdPt/C. The metal nanoparticles in PdFe/C have an average crystallite size of 8.0 nm (Figure 1a). EDX analysis of a randomly sampled nanoparticle in the HRTEM image (Figure 1b) showed the concurrent presence of Pd and Fe in a mole ratio of 70.2:29.8 (Table 1). The carbon-supported PdPtFe alloy nanoparticles with the same overall composition as the core shell nanoparticles also have an average crystallite size of 7.9 nm (Figure 1c). The Pt:Pd:Fe ratio as determined by EDX is 12.1:69.5:18.4 (for the nanoparticle in Figure 1d). The carbon-supported PdFe@PdPt nanoparticles also have a crystallite size of ∼8.1 nm (Figure 1e). EDX measurements showed a greatly depressed Fe content and a relatively constant Pd content (Pt:Pd:Fe = 12.6:68.4:19.0 for the nanoparticle in Figure 1f) relative to the starting PdFe/C confirming the selective etching of Fe (instead of Pd) by the galvanic replacement reaction (one Pt per Fe replaced). To a first approximation, the core shell nanoparticles may be expressed as $Pd_{70}Fe_{30}$@ $Pd_{70}Pt_{30}$. A calculation based on the Benfield model (22) and using the composition of PdFe@PdPt/C from EDX measurements showed that the Fe atoms in first and second outermost layers of PdFe/C have been replaced.

The XRD diffraction patterns of Pt/C, PdFe/C, PdPtFe/C, and PdFe@PdPt/C shown in Figure 2 could all be indexed to the fcc structure. The absence of distinct Fe diffractions in PdFe/C and PdPtFe/C suggests that Fe has been fully incorporated into Pd and PdPt as an alloying element. The

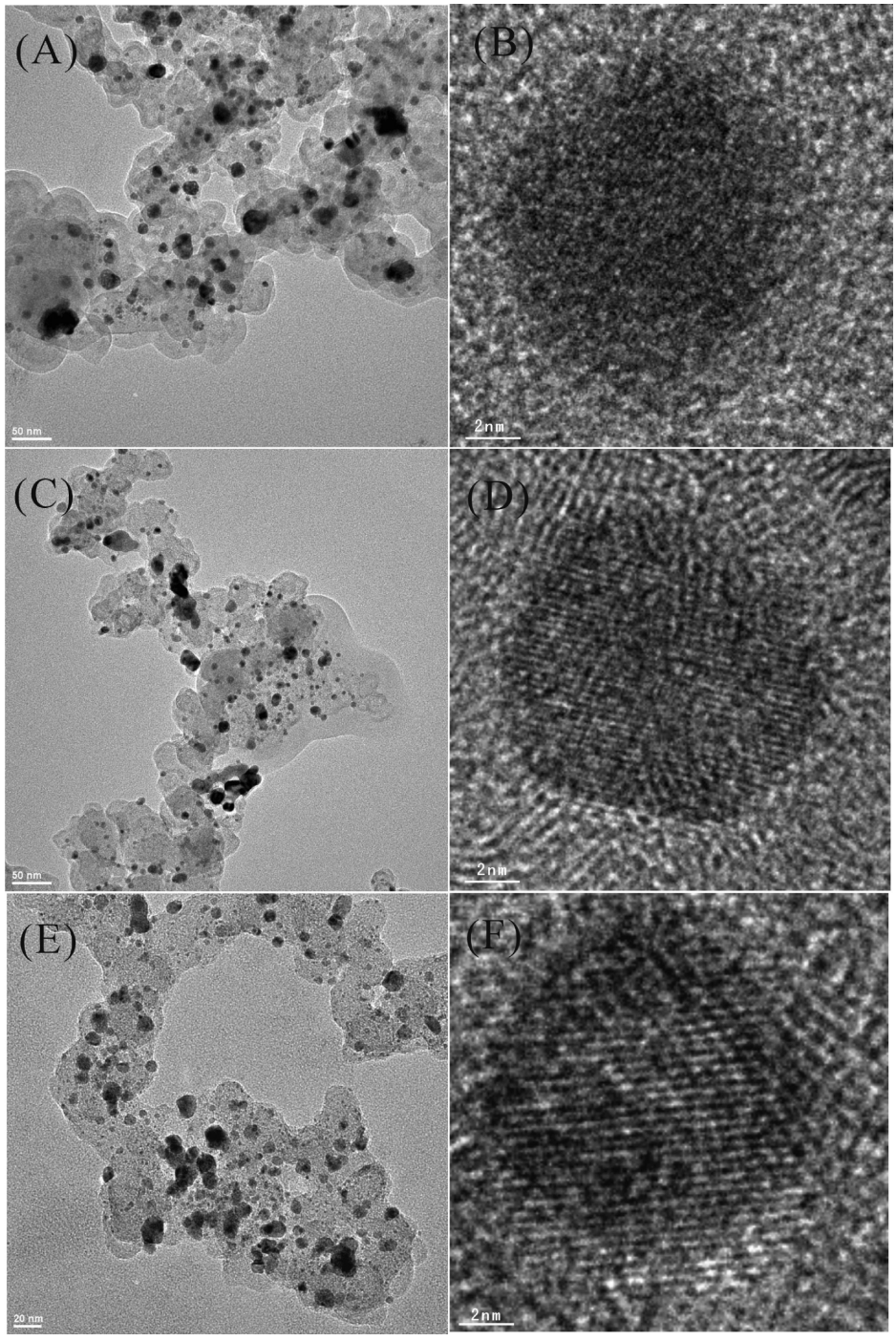

FIGURE 1. TEM images of (a)PdFe/C, (c) PdPtFe/C, and (e) PdFe@PdPt/C, and HRTEM images of (b) PdFe/C, (d) PdPtFe/C, and (f) PdPt@PdFe/C.

Table 1. Atomic Ratios, Crystallite Size and Lattice Parameter and Electrochemical Surface Area of Pt/C, PdFe/C, PdPtFe/C, and PdFe@PdPt/C

catalysts	Pt:Pd:Fe atomic ratios from EDX	mean crystallite size from TEM/XRD (nm)	lattice parameter (Å)	ECSA (m^2 (g of PtPd)$^{-1}$)
Pt/C	100:0:0	3.0[a]/2.9	3.9231	61.1
PdFe/C	0:70.2:29.8	8.0/7.9	3.8705	50.6
PdPtFe/C	12.1:69.5:18.4	7.9/7.8	3.8795	58.8
PdFe@PdPt/C	12.6:68.4:19.0	8.1/8.0	3.8760	72.5

[a] From Figure S1 in the Supporting Information.

(220) diffraction was used to calculate the lattice parameters of the nanoparticles and the crystallite size by the Debye–Scherrer equation (inset of Figure 2 and Figure S2 in the Supporting Information) (23). The summary in Table 1

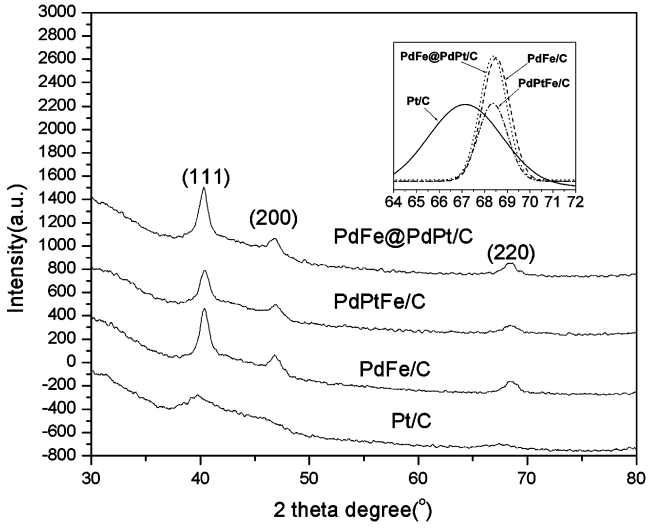

FIGURE 2. XRD patterns of Pt/C, PdFe/C, PdPtFe/C, and PdFe@PdPt/C. The inset shows the enlarged region from (220) diffraction.

shows that the incorporation of Fe into Pd has led to a general contraction of the lattice parameter from 0.38898 nm for Pd to 0.38705 nm for PdFe. The lattice parameter of the PdFe@PdPt nanoparticles at 0.38760 nm also represents a slight contraction from Pd (0.38898 nm) and Pt (0.39231 nm). It is also smaller than the measured lattice parameter of the PdPtFe alloy nanoparticles (0.38795 nm). Indeed, the lattice parameter of PdFe@PdPt is closer to that of PdFe (0.38705 nm) than of PdPt (0.38998 nm). The similarity between the (220) diffractions of PdFe@PdPt/C and PdFe/C confirms that the skin layer is relatively thin, as predicted by the calculation based on the Benfield model (22). The absence of a Pt(220) diffraction (inset of Figure 2) in PdFe@PdPt/C indicates that there were no discrete Pt nanoparticles.

Figure 3 shows the XPS spectra of Pt/C, PdPtFe/C, and PdFe@PdPt/C, with Table 2 summarizing the results of peak deconvolution. In Figure 3a, which shows the Pt 4f region of the Pt/C spectrum, the most intense doublet (at 71.00 and 74.38 eV) is characteristic of metallic Pt. The second and weaker doublet (at 72.55 and 75.53 eV) could be assigned to oxidized Pt in the forms of PtO and $Pt(OH)_2$. For PdPtFe/C, the Pt 4f spectral region in Figure 3b could be deconvoluted into a doublet at 70.50 and 73.85 eV assignable to Pt(0), and a doublet at 72.35 and 75.32 eV due to the Pt oxides. The negative shifts in the Pt 4f signal relative to Pt/C is an indication of electron transfer from the Fe atoms to the neighboring more electronegative Pt atoms. The XPS analysis also measured a Pt: Pd: Fe ratio of 14.5:66.2:19.3. The good agreement with the EDX measurements (12.1:69.5:18.4) indicates homogeneity of composition throughout the particles. For PdFe@PdPt/C, the Pt4f region could be deconvoluted into 71.65 and 74.98 eV for Pt (0), and 73.41 and 76.40 eV for the Pt oxides (Figure 3c). In this case, the Pt 4f signals have shifted positively relative to Pt/C, which is consistent with the compressive strain introduced by depositing a PtPd surface with a larger lattice parameter (0.38998 nm) over a PdFe substrate with a smaller lattice parameter (0.38705 nm) (19, 24). The Pt:Pd:Fe ratio from

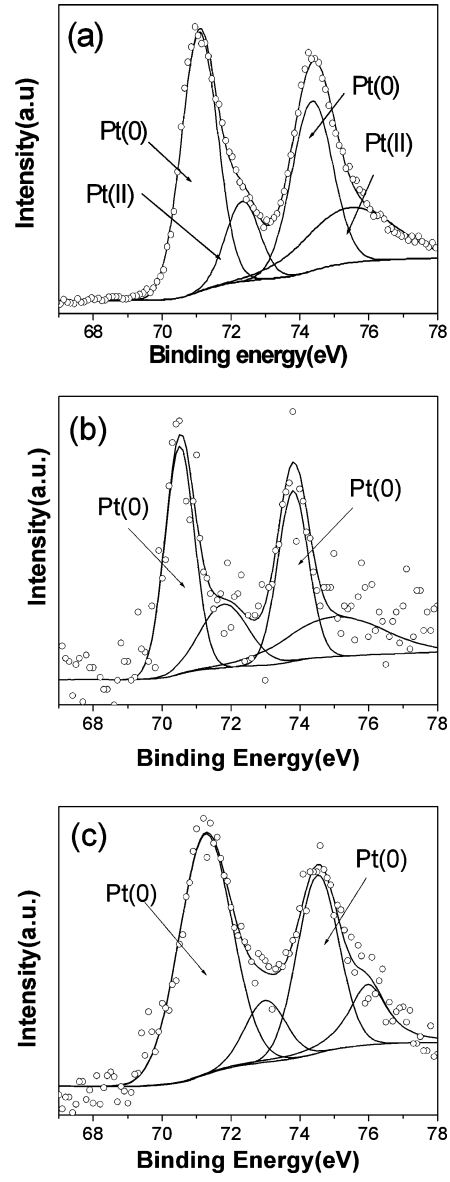

FIGURE 3. Pt 4f XPS spectra of (a) Pt/C, (b) PdPtFe/C, and (c) PdFe@PdPt/C.

XPS analysis is 21.5:65.5:13.0 for PdFe@PdPt/C. Here the Pt content is noticeably higher than that measured by EDX (12.6:68.4:19.0). It is also higher than the XPS measurement of the Pt content in PdPtFe/C alloy nanoparticles (14.5:66.2:19.3), where Pt is homogeneously distributed throughout. These are indications that the PdFe@PdPt/C nanoparticles have a more Pt-rich surface than the surface of the alloy nanoparticles with the same overall composition.

Electrochemical Measurements. Figure 4 shows the cyclic voltammograms of Pt/C, PdFe/C, PdPtFe/C and PdFe@PdPt/C in argon-purged 0.1 M $HClO_4$ at room temperature. The electrochemical surface areas (ECSA) calculated from the hydrogen adsorption/desorption region (0 to 0.30 V) are 61.1 $m^2\ g^{-1}$ for Pt/C, 50.6 $m^2\ g^{-1}$ for PdFe/C, 58.8 $m^2\ g^{-1}$ for PdPtFe/C, and 72.5 $m^2\ g^{-1}$for PdFe@PdPt. In the magnified hydrogen desorption region in Figure 4, two peaks corresponding to hydrogen desorption from Pt (111) and Pt(200) could be identified in the Pt/C sample (25).

Table 2. Atomic Ratios, Chemical State, and Binding Energy of Pt 4f for Pt/C, PdPtFe/C, and PdFe@PdPt/C from XPS Analysis

catalyst	atomic ratio of Pt:Pd:Fe	assigned chemical state	binding energy of Pt 4f 7/2 (eV)	binding energy of Pt 4f 5/2 (eV)	relative intensity (%)
Pt/C	100:0:0	Pt(0)	71.00	74.38	77.8
		Pt oxide	72.55	75.53	22.2
PdPtFe/C	14.5:66.2:19.3	Pt(0)	70.50	73.85	78.9
		Pt oxide	71.80	75.03	21.1
PdFe@PdPt/C	21.5:65.5:13.0	Pt(0)	71.65	74.98	79.4
		Pt oxide	73.41	76.40	20.6

Contrasting this is the single desorption peak in the case of PdFe/C at about 0.18 V. PdPtFe/C and PdFe@PdPt/C also feature single desorption peaks that are noticeably different from hydrogen desorption from monometallic Pt/C and bimetallic PdFe/C. The difference is taken as an indication of the changes in the adsorption site geometry. In the cathodic scan, the oxide (OH_{ads}) stripping peak (735 mV) on PdFe@PdPt/C is located at a potential higher than that of Pt/C (730 mV), PdFe/C (680 mV) and PdPtFe/C (690 mV). The positive shift of the oxide stripping peak on PdFe@PdPt/C suggests weaker binding of the OH_{ads}-species on the surface of the core shell nanoparticles (26).

The catalytic activities of Pt/C, PdFe/C, PdPtFe/C, and PdFe@PdPt/C were measured with a RDE both in the presence and absence of 0.1 M methanol, a typical concentration used in methanol tolerance studies (27, 28). Figure 5a shows the ORR in oxygen-saturated 0.1 M $HClO_4$ at room temperature without methanol. Half-wave potentials of 0.805, 0.760, 0.785, and 0.830 V were measured for Pt/C, PdFe/C, PdPtFe/C, and PdFe@PdPt/C, respectively. The half-wave potential is the most positive for PdFe@PdPt/C (0.830 V), indicating that it is the most active among the catalysts tested. The kinetic mass activity at 0.8 V calculated from the Koutecký-Levich eq (1.92 mA μg^{-1} (Pt) for PdFe@PdPt/C)) is also higher than the value known for nanosized Pt (4). Figure 5b shows the polarization curves in the presence of 0.1 M CH_3OH. In this case, ORR on PdFe/C proceeded normally as in the case without methanol. This is an expected outcome, because Pd alloys are inactive for the methanol oxidization reaction (MOR) and are therefore methanol tolerant catalysts (17, 19). On the other hand, the polarization curves of Pt/C, PdPtFe/C, and PdFe@PdPt/C display current density reversals culminating in "valleys" (minimums current densities) formed around 0.71 V. The current reversal was caused by the competition between methanol oxidization and oxygen reduction on the same

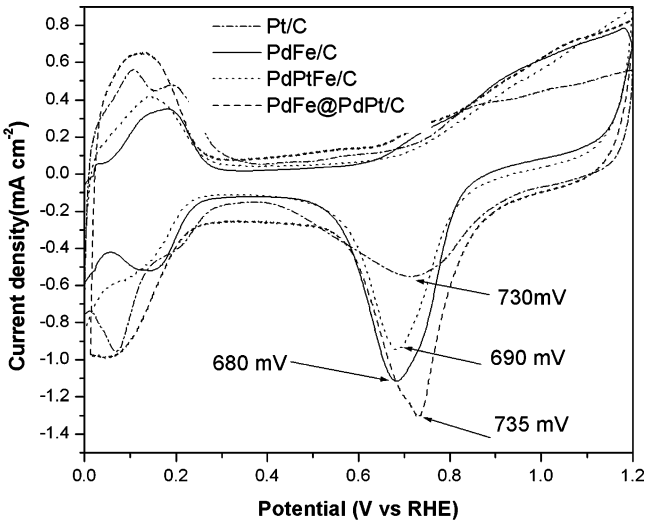

FIGURE 4. Cyclic voltammograms of Pt/C, PdFe/C, PdPtFe/C, and PdFe@PdPt/C in argon-purged 0.1 M $HClO_4$. Sweep rate 20 mV s^{-1}; room temperature.

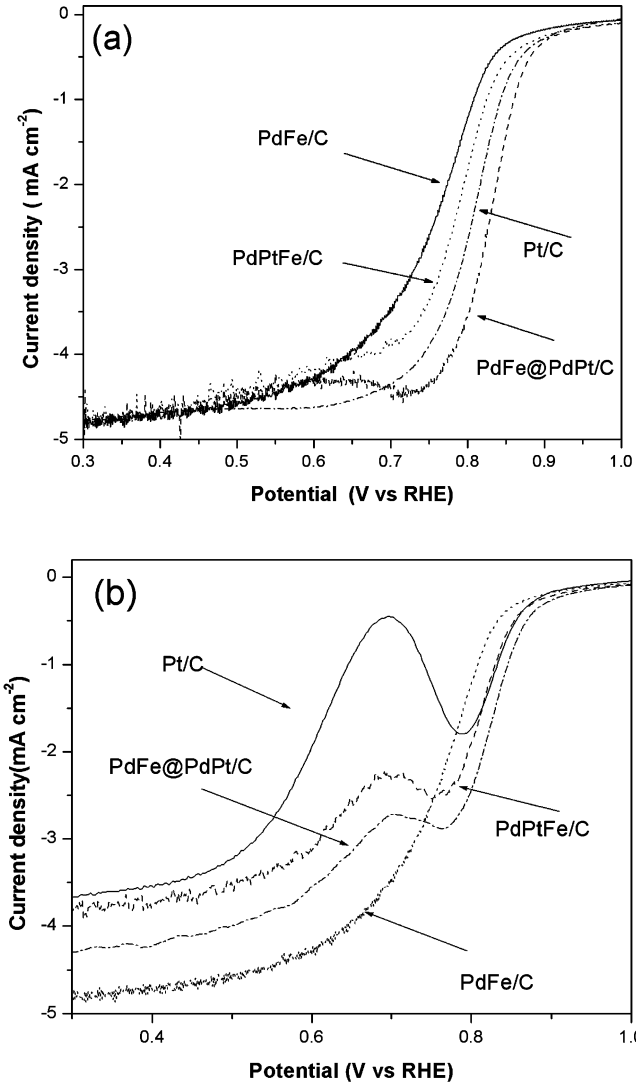

FIGURE 5. Linear voltammograms of Pt/C, PdFe/C, PdPtFe/C, and PdFe@PdPt/C in oxygen-saturated 0.1 M $HClO_4$ (a) without and (b) with 0.1 M CH_3OH in negative-going scans. Sweep rate 20 mV s^{-1}; room temperature; 1600 rpm.

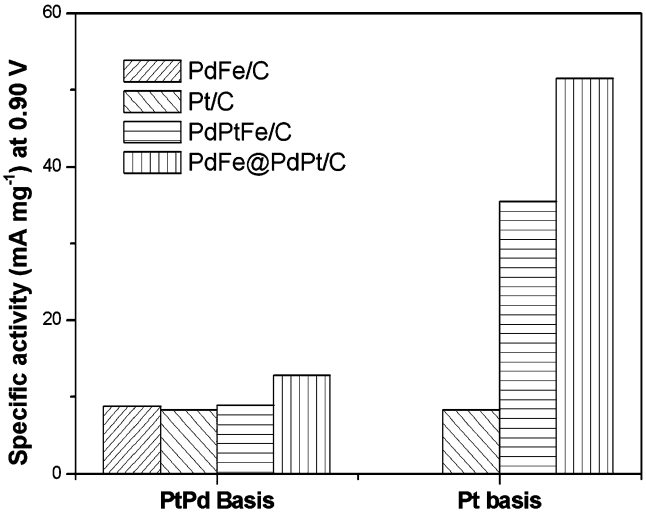

FIGURE 6. Specific activities at 0.9 V vs RHE in the presence of methanol on Pt+Pd or Pt metal basis for Pt/C, PdFe/C, PdPtFe/C, and PdFe@PdPt/C catalysts.

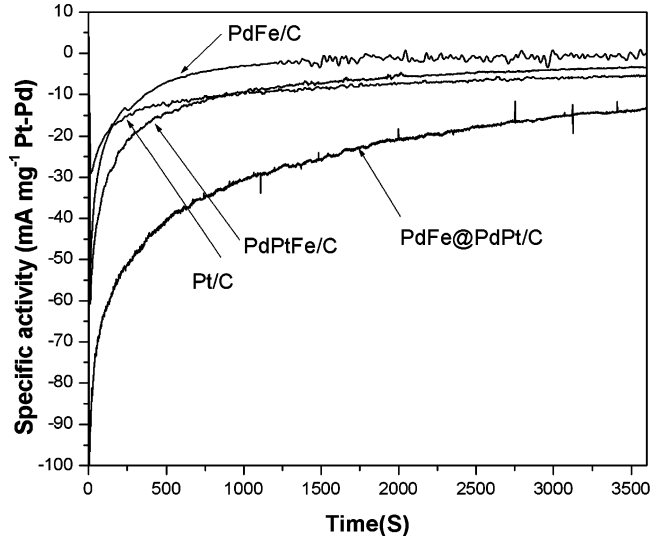

FIGURE 7. Chronoamperograms of Pt/C, PdFe/C, PdPtFe/C, and PdFe@PdPt/C at 0.90 V in oxygen-saturated 0.1 M $HClO_4$ with 0.1 M CH_3OH. Room temperature; 1600 rpm.

reduced Pt surface, resulting in the negation of the ORR current by the MOR current. Among the Pt-containing catalysts, the ORR activity of PdFe@PdPt/C is the least affected in the presence of methanol, comfortably outperforming PdPtFe/C and Pt/C, especially in the high potential region (>0.8 V).

The enhancement of ORR activity through a core shell construction may be understood in terms of the ligand effect and the lattice strain effect in catalysi s (29). The ligand effect, which concerns the electron transfer from the oxophilic metal (Fe) to the noble metals (Pd, Pt) (30), is generally less effective than the strain effect in changing the d band centers of the surface catalytic metals, which determine the general adsorptive behavior of the catalytic surface (8, 31). The dissociation of the O−O bond in an oxygen molecule on the catalyst surface and the removal of the OH groups subsequently formed are key steps in ORR (9, 32, 33). For Pt-based catalysts, the persistence of the OH groups on the catalyst is the rate-limiting step and adversely affects the ORR activity (9, 32−34). A downward shift in the d-band centers of Pt and Pd would generally weaken the adsorption strength, facilitating the removal of the OH groups and improving the ORR activity as a result. When Pt (0.39231 nm) and Pd (0.38898 nm) with the larger lattice parameters are deposited on PdFe/C with a smaller lattice parameter (0.38705 nm), the Pt and Pd atoms would be laterally compressed compared to their bulk form, lowering their d band centers. The experimental observation of a higher XPS Pt binding energy in core shell PdFe@PdPt/C nanoparticles than in Pt/C nanoparticles (Table 2) is one of the consequences of the downward shift in the d band center. The correlation between binding energy shift and the shift in the d band center has been witnessed before and verified by many others (5, 24, 35).

As a measure of relative methanol tolerance, the specific activities of Pt/C, PdFe/C, PdPtFe/C, and PdFe@PdPt/C at 0.90 V in the presence of methanol are compared based on the total mass of noble metals (Pd+Pt) (Figure 6). When the commercial E-TEK Pt/C catalyst was used in the presence of 0.1 M methanol, a specific activity of 8.4 mA mg^{-1} was measured, which agrees well with the literature value. For PdFe/C and PdPtFe/C, the specific activities are 8.8 mA (mg of (Pd+Pt))$^{-1}$and 8.9 mA (mg of (Pd+Pt))$^{-1}$, respectively. Specific activity is the highest for PdFe@PdPt/C, 12.8 mA mg^{-1}(Pd+Pt), qualifying the core shell structured PdFe@PdPt/C as the most methanol tolerant among the ORR catalysts tested. The good methanol tolerance of heterogeneous PdFe@PdPt/C relative to Pt/C could also be attributed to the presence of Pd on the catalyst surface. Pd and its alloys are known for their methanol tolerance when used as the cathode catalyst for DMFC (17, 19). Therefore, the presence of Pd sites on the catalyst surface ensures methanol tolerance to some extent. Second, the presence of Pd in the surface dilutes the surface Pt sites. For MOR to occur, three adjacent Pt sites are required whereas only two are needed for ORR (36). The three types of bimetallic sites that are expected to be present on the PdFe@PdPt/C catalyst surface, namely Pt−Pt, Pd−Pd, and Pt−Pd, are all ORR-active. The Pd dilution effect therefore affects mostly MOR because of the more demanding site requirement for this reaction. By comparison, the PdPtFe/C catalyst is not as methanol tolerant as PdFe@PdPt/C because the presence of Fe on the surface of the former could enhance MOR via the mechanism of bifunctional catalysis between the noble metals (Pt) and the oxophilic metal (Fe) (37). Moreover, as shown in Figure 6, when Pt-only is used as the basis for normalizing the measured currents, the PdFe@PdPt/C catalyst also shows the highest mass activity in 0.1 M methanol (8.4 mA (mg of Pt)$^{-1}$ for Pt/C, 35.5 mA (mg of Pt)$^{-1}$ for PdPtFe/C, and 51.5 mA (mg of Pt)$^{-1}$ for PdFe@PdPt/C), indicating the more efficient use of Pt via the core shell construction.

Specific activity−time curves measured at a fixed potential were used to assess the long-term catalyst performance. From the chronoamperograms of Pt/C,

PdFe/C, PdPtFe/C, and PdFe@PdPt/C at 0.90 V in oxygen-saturated 0.1 M $HClO_4$ with 0.1 M CH_3OH (Figure 7), specific activities of Pt/C, PdFe/C, and PdPtFe/C decreased to about 5.54, 1.00, and 3.78 mA (mg of (Pd+Pt))$^{-1}$, respectively, after 1 h, whereas the activity of PdFe@PdPt/C after 1 h is noticeably higher (12.88 mA (mg of (Pd+Pt))$^{-1}$, and is about 2.3 times that of Pt/C. A figure of merit (FOM) based on the turnover frequency per Pt atom could be used to compare the effectiveness of the Pt atoms on Pt/C, bulk alloy PdPtFe/C, and heterogeneous core shell PdFe@PdPt/C, and this was calculated by the expression in eq 1. The following values of FOM were obtained for the various catalysts: Pt/C, 2.33×10^{-17} mA cm^{-2} per Pt atom; PdPtFe/C, 2.15×10^{-16} mA cm^{-2} per Pt atom; and PdFe@PdPt/C, 2.75×10^{-16} mA cm^{-2} per Pt atom. The highest FOM of heterogeneous Pt-PdFe/C again confirms the more efficient use of the catalytic noble metal Pt in core shell construction.

$$\mathrm{FOM} = \frac{I}{\pi D_{\text{nano particle}}^2 KX \dfrac{M}{\rho \times \dfrac{4}{3}\pi\left(\dfrac{D_{\text{nano particle}}}{2}\right)^3}} \quad (1)$$

where I is the steady state current of bulk alloy PdPtFe/C, core shell PdFe@PdPt/C, or Pt/C; D is the nanoparticle diameter; K is the surface density of polycrystalline Pt; X is percentage of Pt on the surface; M is the mass loading of metals on the electrode; and ρ is average density of the nanoparticles.

We have therefore shown experimentally that the ORR activity and stability of Pt in the presence of methanol could be enhanced through the core shell PdFe@PdPt/C construction, surpassing the performance of Pt/C catalyst and PdPtFe/C alloy catalyst with the same overall composition. However, it is recognized that the present design of core shell PdFe@PdPt/C may not be optimal because we have explored only a limited number of core shell compositions. In addition, designs may also be based on different combinations of metals. It is hoped that this report could generate sufficient interest to result in more studies in this direction.

CONCLUSION

Carbon-supported Pt-decorated PdFe (PdFe@PdPt/C) nanoparticles with a PdPt surface and a PdFe core were prepared by the galvanic reaction between PdFe/C alloy nanoparticles and $PtCl_4^{2-}$. The absence of Pt (220) diffraction in XRD pattern of PdFe@PdPt/C indicates that there were no discrete Pt nanoparticles. The similarity between PdFe@PdPt/C and PdFe/C diffractions suggests that the compositional deviation from the bulk was limited to a very thin surface layer. XPS nevertheless detected a Pt enriched surface, and the positive shift in the Pt 4f signals relative to Pt/C indicates that the surface layer was under compressive stress relative to the bulk. The PdFe@PdPt/C nanoparticles are active in the oxygen reduction reaction in the presence of 0.1 M methanol. Indeed, they are 2.3 times as active as a reference Pt catalyst with 4 times as much of Pt under the same test conditions. The enhanced ORR activity of PdFe@PdPt/C relative to Pt/C could be understood in terms of a favorable strain effect when Pt is deposited on the PdFe substrate. The presence of Pd on the catalyst surface also contributed to the observed good methanol tolerance.

Acknowledgment. This research is supported by an academic research grant from the Ministry of Education (R279-000-210-112). J.H.Y. also acknowledges the National University of Singapore for his research scholarship.

Supporting Information Available: Additional TEM image of Pt/C; XRD patterns of Pd/C and PdPt/C; linear voltammograms of PdFe@PdPt/C with other compositions in oxygen-saturated 0.1 M $HClO_4$ (PDF). This material is available free of charge via the Internet at http://pubs.acs.org.

REFERENCES AND NOTES

(1) Greeley, J.; Jaramillo, T. F.; Bonde, J.; Chorkendorff, I. B.; Norskov, J. K. *Nat. Mater.* **2006**, *5*, 909–913.
(2) Greeley, J.; Mavrikakis, M. *Nat. Mater.* **2004**, *3*, 810–815.
(3) Zambelli, T.; Barth, J. V.; Wintterlin, J.; Ertl, G. *Nature* **1997**, *390*, 495–497.
(4) Adzic, R. R.; Zhang, J.; Sasaki, K.; Vukmirovic, M. B.; Shao, M.; Wang, J. X.; Nilekar, A. U.; Mavrikakis, M.; Valerio, J. A.; Uribe, F. *Top. Catal.* **2007**, *46*, 249–262.
(5) Alayoglu, S.; Nilekar, A. U.; Mavrikakis, M.; Eichhorn, B. *Nat. Mater.* **2008**, *7*, 333–338.
(6) Stamenkovic, V. R.; Fowler, B.; Mun, B. S.; Wang, G. F.; Ross, P. N.; Lucas, C. A.; Markovic, N. M. *Science* **2007**, *315*, 493–497.
(7) Luo, J.; Wang, L.; Mott, D.; Njoki, P. N.; Lin, Y.; He, T.; Xu, Z.; Wanjana, B. N.; Lim, I. I. S.; Zhong, C. J. *Adv. Mater.* **2008**, *20*, 4342–4347.
(8) Kibler, L. A.; El-Aziz, A. M.; Hoyer, R.; Kolb, D. M. *Angew. Chem., Int. Ed.* **2005**, *44*, 2080–2084.
(9) Zhang, J. L.; Vukmirovic, M. B.; Xu, Y.; Mavrikakis, M.; Adzic, R. R. *Angew. Chem., Int. Ed.* **2005**, *44*, 2132–2135.
(10) Stamenkovic, V. R.; Mun, B. S.; Mayrhofer, K. J. J.; Ross, P. N.; Markovic, N. M. *J. Am. Chem. Soc.* **2006**, *128*, 8813–8819.
(11) Bligaard, T.; Norskov, J. K. *Electrochim. Acta* **2007**, *52*, 5512–5516.
(12) Neergat, M.; Friedrich, K. A.; Stimming, U. *Handbook of Fuel Cells: Fundamentals, Technology, and Applications*; Vielstick, W., Gasteiger, H., Lamm, A., Eds.; John Wiley& Sons: New York, 2003; Vol. 4, p 845.
(13) Arico, A. S.; Srinivasan, S.; Antonucci, V. *Fuel Cells* **2001**, *1*, 1–29.
(14) Srivastava, R.; Mani, P.; Hahn, N.; Strasser, P. *Angew. Chem., Int. Ed.* **2007**, *46*, 8988–8991.
(15) Jaouen, F. d. r.; Herranz, J.; Lefèvre, M.; Dodelet, J.-P.; Kramm, U. I.; Herrmann, I.; Bogdanoff, P.; Maruyama, J.; Nagaoka, T.; Garsuch, A.; Dahn, J. R.; Olson, T.; Pylypenko, S.; Atanassov, P.; Ustinov, E. A. *ACS Appl. Mater. Interfaces* **2009**, *1*, 1623–1639.
(16) Shao, M. H.; Sasaki, K.; Adzic, R. R. *J. Am. Chem. Soc.* **2006**, *128*, 3526–3527.
(17) Shao, M. H.; Huang, T.; Liu, P.; Zhang, J.; Sasaki, K.; Vukmirovic, M. B.; Adzic, R. R. *Langmuir* **2006**, *22*, 10409–10415.
(18) Lee, K.; Savadogo, O.; Ishihara, A.; Mitsushima, S.; Kamiya, N.; Ota, K. *J. Electrochem. Soc.* **2006**, *153*, A20–A24.
(19) Li, H. Q.; Xin, Q.; Li, W. Z.; Zhou, Z. H.; Jiang, L. H.; Yang, S. H.; Sun, G. Q. *Chem. Commun.* **2004**, *23*, 2776–2777.
(20) Hayre, R. O.; Cha, S. W.; Colella, W.; Prinz, F. B. *Fuel Cell Fundamentals*; John Wiley& Sons: New York, 2006.
(21) Bard, A. J.; Parsons, R.; Jordan, J. *Standard Potentials in Aqueous Solutions*; Marcel Dekker: New York, 1985.
(22) Benfield, R. E. *J. Chem. Soc., Faraday Trans.* **1992**, *88*, 1107–1110.
(23) Radmilovic, V.; Gasteiger, H. A.; Ross, P. N. *J. Catal.* **1995**, *154*, 98–106.
(24) Richter, B.; Kuhlenbeck, H.; Freund, H. J.; Bagus, P. S. *Phys. Rev. Lett.* **2004**, *93*, 026805(1)−026805(4) .
(25) Wang, C.; Daimon, H.; Onodera, T.; Koda, T.; Sun, S. H. *Angew. Chem., Int. Ed.* **2008**, *47*, 3588–3591.

(26) Gasteiger, H. A.; Kocha, S. S.; Sompalli, B.; Wagner, F. T. *Appl. Catal., B* **2005**, *56*, 9–35.
(27) Antolini, E.; Lopes, T.; Gonzalez, E. R. *J. Alloys Compd.* **2008**, *461*, 253–262.
(28) Kin, T. H.; Shieh, W. Y.; Yang, C. C.; Yu, G. *J. Power Sources* **2006**, *161*, 1183–1186.
(29) Kitchin, J. R.; Norskov, J. K.; Barteau, M. A.; Chen, J. G. *Phys. Rev. Lett.* **2004**, *93*, 156801(1)−156801(4) .
(30) Luna, A. M. C.; Bonesi, A.; Triaca, W. E.; Baglio, V.; Antonucci, V.; Arico, A. S. *J. Solid State Electrochem.* **2008**, *12*, 643–649.
(31) Kumar, S.; Zou, S. Z. *Langmuir* **2007**, *23*, 7365–7371.
(32) Kinoshita, K. *Electrochemical Oxygen Technology*; Wiley: New York, 1992.
(33) Markovic, N.; Gasteiger, H.; Ross, P. N. *J. Electrochem. Soc.* **1997**, *144*, 1591–1597.
(34) Markovic, N. M.; Ross, P. N. *Surf. Sci. Rep.* **2002**, *45*, 121–229.
(35) Zhou, W. P.; Lewera, A.; Larsen, R.; Masel, R. I.; Bagus, P. S.; Wieckowski, A. *J. Phys. Chem. B* **2006**, *110*, 13393–13398.
(36) Salgado, J. R. C.; Antolini, E.; Gonzalez, E. R. *Appl. Catal., B* **2005**, *57*, 283–290.
(37) Liu, F.; Lee, J. Y.; Zhou, W. J. *Small* **2006**, *2*, 121–128.

AM900623E